Electrochimica Acta 430 (2022) 141047

Contents lists available at ScienceDirect

Electrochimica Acta

journal homepage: www.journals.elsevier.com/electrochimica-acta

Investigating the particle size effect on the electrochemical performance and degradation of cobalt-free lithium-rich layered oxide $Li_{1.2}Ni_{0.2}Mn_{0.6}O_2$

Hyeongseon Choi [a,b], Annika Regitta Schuer [a,b], Hyein Moon [a,b], Matthias Kuenzel [a,b,*], Stefano Passerini [a,b,*]

[a] Helmholtz Institute Ulm (HIU) Electrochemical Energy Storage, Helmholtzstrasse 11, 89081 Ulm, Germany
[b] Karlsruhe Institute of Technology (KIT), P.O. Box 3640, 76021 Karlsruhe, Germany

ARTICLE INFO

Keywords:
Cobalt-free
High capacity
Cathode active materials
Co-precipitation chemistry
Lithium-rich Mn-rich layered oxide

ABSTRACT

Lithium-rich layered oxides (LRLOs) as Li-ion battery positive electrode materials promise to deliver superior specific capacity (> 270 mAh g^{-1}) boosting the driving range of electric vehicles (EVs). Interestingly, these materials do not strictly require cobalt in their formulation, solving the supply, environmental, and ethical issues associated to this metal. Herein the synthesis of Co-free $Li_{1.2}Ni_{0.2}Mn_{0.6}O_2$ (LRNM) via lab-scale co-precipitation and solid-state reaction is reported, employing transition metal salts with different anions. These yield to different morphological features of the resulting LRNMs, also impacting the physicochemical characteristics and electrochemical performance. The use of sulfate TMs results in a material (LRNM-S) with smaller crystallite and particle sizes, which displays very high specific capacity (more than 270 mAh g^{-1} at C/20) and excellent rate capability (109 mAh g^{-1} at 10C). However, its capacity and voltage fading are also more pronounced than for the acetate-based material (LNRM-A), which owns twice as large crystallites achieving capacity and voltage retention both higher than 97% over 100 cycles. Our investigation unveiled the prevalent trade-off between full activation and exploitation of the LRLOs high specific capacity and anion redox against structural degradation and accelerated ageing of the materials.

1. Introduction

Lithium-ion batteries (LIB) are probably the top (electro)chemical achievement fulfilling the portable energy storage needs of our society. With their exceptional specific energy density and offering rapid dis-/charge rates, LIBs have become increasingly important for portable applications like cell phones, laptops and other smart devices, and, even more crucially, for electric mobility ranging from hybrid (HEVs) over plug-in hybrid (PHEVs) to full electric vehicles (EVs) [1,2]. Enhancing the performance of the positive electrode (cathode) is a key goal for the realization of reliable LIB cells [3–5]. Positive active materials in LIBs are mostly based on transition metal oxides or phosphates such as $LiCoO_2$ (LCO), $LiNi_xCo_yMn_zO_2$ (NCM_{xyz}), $LiNi_xCo_yAl_zO_2$ (NCA_{xyz}), $LiMn_2O_4$ (LMO), $LiNi_{0.5}Mn_{1.5}O_4$ (LNMO), and $LiFePO_4$ (LFP). However, they either contain environmentally and economically critical elements, i.e., cobalt [6–8], or cannot provide sufficient energy density for EV applications [9]. Nonetheless, one class of materials, i.e., lithium-rich layered oxides (LRLOs) composed of Ni and Mn, exists, and promises to fulfil the sustainability and performance criteria: 1) Sourcing and synthesis of the active materials without critical elements and 2) high specific capacity and energy density required for advanced EV technologies. In particular, these cobalt-free materials share the formula $Li_{1+x}(Ni_aMn_b)_{1-x}O_2$ (x >0; a + b = 1) LRNM [10].

The excess of lithium available in LRLOs directly translates into a much larger specific discharge capacity (> 270 mAh g^{-1}) compared to conventional stoichiometric layered oxide materials [11,12]. This outstanding capacity is originating from the structural ambiguity of LRLOs consisting of two phases, $LiMO_2$ and Li_2MnO_3, which however is also causing serious obstacles for commercialization of this class of materials, i.e., poor kinetics, large voltage hysteresis and substantial voltage and capacity decay upon cycling [13–15]. The coexistence of a stoichiometric layered structure of $LiMO_2$ (M = Ni, Mn, Co or Al) and a Li_2MnO_3 phase in LRLOs is enabled by their structural similarity [16–18]. Following this peculiarity, the first charge profile of LRLOs is distinguishingly composed of two regions where different components are electrochemically active. Up to about 4.35 V the profile appears with

* Corresponding authors at: Helmholtz Institute Ulm (HIU) Electrochemical Energy Storage, Helmholtzstrasse 11, 89081 Ulm, Germany.
E-mail addresses: matthias.kuenzel@kit.edu (M. Kuenzel), stefano.passerini@kit.edu (S. Passerini).

https://doi.org/10.1016/j.electacta.2022.141047
Received 12 April 2022; Received in revised form 14 August 2022; Accepted 14 August 2022
Available online 15 August 2022

a continuous slope associated to the classic redox of transition metal cations: Co^{3+}/Co^{4+} and $Ni^{2+}/Ni^{3+}/Ni^{4+}$, while Mn^{4+} as structural stabilizer maintains its oxidation state. At higher potential (> 4.35 V) the shape changes into an extended plateau where the Li_2MnO_3 phase is activated involving partially irreversible oxygen redox ($O^{2-} \rightarrow O^{(2+x)-} + x\bullet e^-$), oxygen loss from the lattice and in the worst case O_2 evolution from the structure [15,19,20]. At the surface of the active material particles oxygen is easily lost irreversibly, triggering the dislocation of transition metal ions which are subsequently trapped in the lithium sites. This process, referred to as cation mixing or lattice densification, results in the formation of a surface reconstruction layer affecting Li-ion diffusion and re-intercalation. Accumulated over many cycles, the layered structure transforms into a spinel-like phase and, eventually, the electrochemically inactive rock-salt structure. This irreversible structural transformation is one of the main causes leading to the voltage fade and capacity decay deteriorating the electrochemical performance of LRLOs during long-term cycling [21–23].

In this regard, the choice of synthesis methods critically influences the properties and electrochemical performance of lithium-ion cathodes. Direct solid-state synthesis is one of the most known and longest established method to prepare active materials for LIBs with the advantage of easily achieving the correct stoichiometry. However, it comes with extra-costs deriving from the long calcination step at elevated temperature and difficulties in handling the scale-up to large quantities. For such a reason, co-precipitation has become the most employed synthesis route recently thanks to its simplicity, scalability, and homogeneous atomic-level mixing of the composing elements in the precursor. These are the primary advantages of co-precipitation allowing for the heat treatment to be performed at lower temperatures and shorter times. Depending on the typical transition metal sources and reactant precursors, co-precipitation routes can be classified into transition metal hydroxides ($TM(II)(OH)_2$), carbonates ($TM(II)CO_3$) and oxalates ($TM(II)C_2O_4$, TM = Mn, Ni, Co and Al). The counter ion bound in the transition metal source also influences the characteristics of the precursors as well as the final products [24]. Various reports regarding acetates (-CH_3COO) [25,26], sulfates (-SO_4) [27–29] and nitrates (-NO_3) [30,31] to synthesize LRLO precursor materials are also available. However, to the best of our knowledge, there is no report comparing two different co-precipitation chemistries and the electrochemical performance of the resulting LRLOs.

In this work, two different chemistries to prepare hydroxide precursors, involving the co-precipitation of either sulfates ($TM(II)SO_4\bullet nH_2O$, TM = Mn and Ni) or acetates ($TM(II)(CH_3COO)_2\bullet nH_2O$) with $LiOH\bullet H_2O$, followed by solid-state reaction to prepare the final lithium-rich layered oxide, are compared to investigate how different transition metal sources impact the properties and electrochemical performance of $Li_{1.2}Ni_{0.2}Mn_{0.6}O_2$ (LRNM).

2. Experimental

2.1. Synthesis

Various $Li_{1.2}Ni_{0.2}Mn_{0.6}O_2$ (LRNM) active materials were synthesized by hydroxide co-precipitation and high-temperature solid-state reaction. Precursor materials, $Ni_{0.2}Mn_{0.6}(OH)_{1.6}$ were prepared from two different transition metal sources, but employing the same conditions, i.e., 1M concentration of reactant and transition metal solutions, room temperature (~25 °C) and under constant argon flow (inert atmosphere). Stoichiometric amounts of either manganese sulfate tetrahydrate ($Mn(II)SO_4\bullet 4H_2O$) and nickel sulfate tetrahydrate ($Ni(II)SO_4\bullet 4H_2O$) or manganese acetate tetrahydrate ($Mn(II)(CH_3COO)_2\bullet 4H_2O$) and nickel acetate monohydrate ($Ni(II)(CH_3COO)_2\bullet H_2O$) as starting materials were dissolved in deionized water (Solution A) at 1M concentration. The precipitation agent, i.e., the 1M lithium hydroxide monohydrate ($LiOH\bullet H_2O$) aqueous solution (Solution B), was placed in a three neck round flask. Under vigorous stirring and argon flow, Solution A was added dropwise into Solution B over a period of 120 minutes. The mixture was aged overnight (~ 16 h) to yield the hydroxide precursor. The precipitate was vacuum-filtered and rinsed with deionized water until neutralization (pH = 7). Washed products were dried in an atmospheric oven at 80 ºC to remove residual moisture overnight, then ground and thoroughly mixed by ball-milling for 5 hours using acetone as dispersant with $LiOH\bullet H_2O$. This latter was added in excess of 2.5 mol % (i.e., 1.23 equivalents with respect to $Ni_{0.2}Mn_{0.6}(OH)_{1.6}$) to compensate for the lithium loss during the high temperature calcination step. The dried mixture was calcined in the box furnace at 480 °C for 5 h and pelletized into round disks. Pellets were fired at 900 °C for 24 h and directly quenched into liquid nitrogen (N_2) followed by grinding and sieving to obtain fine (< 45 μm) powders of LRNM materials.

2.2. Electrode preparation

Positive electrode sheets were prepared by spreading a slurry mixture of the as-prepared LRNM active materials, conductive carbon Super C65 (IMEYRS) and polyvinylidene difluoride (PVdF, Solef 5130, Solvay) in mass ratio of 85:10:5 on the aluminum foil current collector. PVdF binder was dissolved in N-methyl-2 pyrrolidone (NMP) as a 4 wt% solution beforehand. Dried electrode sheets were punched in circular shape (Ø = 12 mm). The electrode disks were pressed for 10 s at 10 ton cm^{-2} and dried in dynamic vacuum at 120 °C for 16 h before being transferred into an argon-filled glove box (MB200B ECO, MBraun; O_2 < 0.1 ppm, H_2O < 0.1 ppm). The active material mass loading of the electrodes ranged between 3.5 and 4.0 mg cm^{-2}.

2.3. Electrochemical measurements

Three-electrode half-cells were assembled inside T-shaped Swagelok connectors, using an LRNM disk as the working electrode and lithium metal foils as counter and reference electrodes. To prevent short circuiting of the electrodes, two glass fiber separators (Whatman GF/D Ø = 13 mm between working/counter, Ø = 10 mm towards the reference electrode) soaked with 240 μL of the electrolyte (1M $LiPF_6$ in ethyl carbonate (EC)/dimethyl carbonate (DMC), 1:1 w/w, LP30, Solvionic) were used.

The galvanostatic charge/discharge tests were performed using a battery tester (Maccor 4300). The nominal specific capacity of 250 mAh g^{-1} was adopted to define the specific current rate of 1C. The rate capability of the electrodes within the 2.5 and 4.8 V voltage limits was evaluated according to the following procedure. First, an activation cycle at 0.05 C was performed followed by 5 cycles at various dis-/charge rates (up to 10C). The long-term cycling stability was assessed at 1C between 2.5 and 4.6 V after the activation cycle at 0.05C with an anodic cut-off voltage of 4.8 V. All electrochemical characterizations were carried out in a climatic chamber at 20 ± 2 °C.

2.4. Materials characterization

The chemical composition of the as-prepared samples was determined by inductively coupled-plasma optical emission spectroscopy (ICP-OES) measurements on a Spectro Arcos spectrometer (Spectro Analytical Instruments) after dissolving the sample in *aqua regia*. For the structural and crystallographic investigation of the samples, X-ray powder diffraction (XRD) was performed (Bruker D8 Advance diffractometer, Cu Kα radiation, λ = 0.154 nm) in the range of 10 < 2θ < 90° with a step size of 0.02° and 6.5 s. per step recording time. Rietveld refinements were performed using Topas Academic. A Chebychev background was fitted and the instrumental resolution was characterized using the Thompson-Cox-Hastings function. The active material morphology was investigated via scanning electron microcopy (SEM) utilizing a Zeiss Crossbeam 340 field-emission electron microscope at an acceleration voltage of 3 kV.

X-ray photoelectron spectroscopy (XPS) measurements were carried

Table 1
Atomic composition as targeted and found for LRNM-S and LRNM-A.

	Targeted	LRNM-S	LRNM-A
Mn:Ni ratio	3	3.14	3.12
Li:(Mn+Ni) ratio	1.5	1.61	1.49

out on fresh and cycled electrodes using a Phoibos 150 XPS spectrometer equipped with a micro-channel plate and in Delay Line Detector (DLD) employing a monochromatic Al Kα ($h\nu = 1486.6$ eV) X-ray source. X-ray source power, pass energy and energy steps were fixed at 400 W (15 kV), 30 eV and 0.1 eV, respectively for Fixed Analyzer Transmission mode. Deconvolution of the detail spectra was performed using the CasaXPS software with a non-linear Shirley-type background and 70 % Gaussian and 30 % Lorentzian profile functions. All spectra were calibrated to the C═C peak in the C1s region at 248.4 eV.

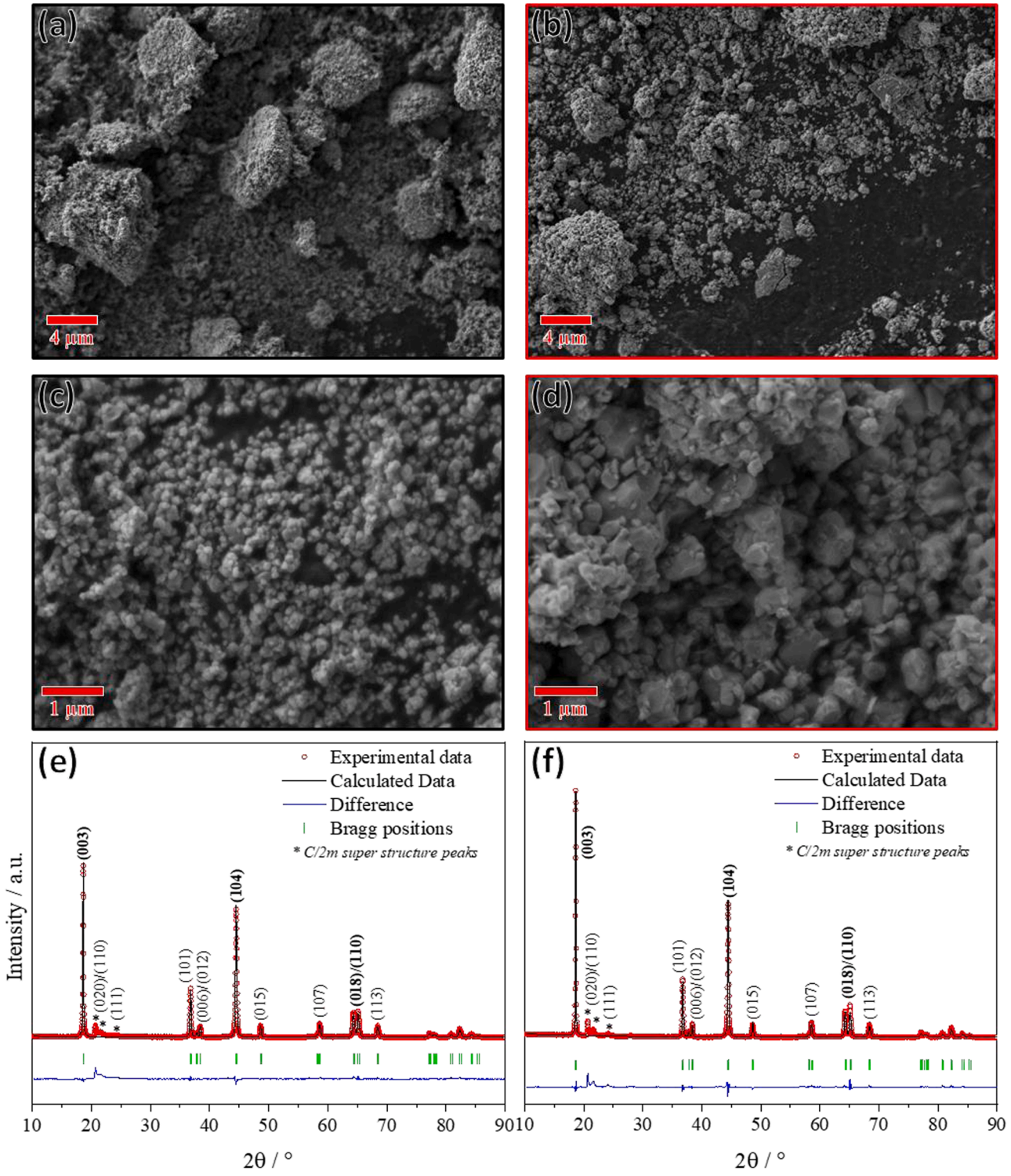

Fig. 1. SEM micrographs of (a,c) LRNM-S and (b,d) LRNM-A at different magnifications. Rietveld refinement of (e) LRNM-S and (f) LRNM-A powder XRD patterns.

Table 2
Refined structural parameters from the XRD patterns of LRNM-S and LRNM-A.

	LRNM-S	LRNM-A
Crystal system	Trigonal	Trigonal
Space group	R-3m	R-3m
Lattice parameter a, b (Å)	2.86	2.86
Lattice parameter c (Å)	14.26	14.28
Unit volume (Å^3)	101.17	101.38
Crystallite size (nm)	**130**	**224**
Cation mixing (Ni^{2+} in Li^+ layer)	6 %	5 %
Phase density (g cm^{-3})	4.14	4.19

All *ex-situ* measurements (XRD and XPS) were performed on the same working electrodes recovered from the half-cells after a selected number of dis-/charge cycles. For this purpose, the cells were disassembled in the argon-filled glove box. The recovered positive electrodes were washed carefully with DMC solvent to remove residuals of the electrolyte. Subsequently, the electrodes were cut into four pieces and specific sample holders were used for their transfer into the respective instruments in order to avoid any contact of the electrodes to ambient atmosphere.

3. Results and discussions

Two different co-precipitation chemistries were selected to prepare $Mn_{0.6}Ni_{0.2}(OH)_{1.6}$ precursors. The composition of the resulting materials, denoted as LRNM-S if derived from TM sulfates or LRNM-A if derived from TM acetates, in terms of atomic ratios of lithium, manganese and nickel is given in Table 1. Although the same excess of lithium source was added to both precursors, the lithium to TM ratio is slightly higher for LRNM-S than for LRNM-A, resulting in slightly different nominal stoichiometries of $Li_{1.23}Ni_{0.19}Mn_{0.58}O_2$ (LRNM-S) and $Li_{1.20}Ni_{0.20}Mn_{0.61}O_2$ (LRNM-A). Both samples show a slight deficiency in nickel as the Mn to Ni ratio exceeds the targeted value of 3.

With regard to morphology, both LRNM-S and LRNM-A show primary particles agglomerated into secondary particles (Fig. 1). The lower magnification micrographs in Fig. 1(a,b) reveal that the secondary particles of both materials have rather irregular shape and size, the latter ranging from less than 1 μm to around 10 μm. At higher magnification (Fig. 1(c,d)) the morphological differences between the two materials become more obvious. LRNM-S shows relatively more homogeneous shape and size and overall smaller primary particles, whereas LRNM-A shows primary particle of various appearance and with sharp edges. These differences indicate that the anion of the transition metal salts strongly affects the morphology of the synthesized LRNM despite the otherwise identical synthesis procedure. Fig. 1(e,f) displays the refined powder XRD patterns of LRNM-S and LRNM-A, which confirm that both samples have essentially the identical trigonal structure of R-3m space group. The reflections between 20 °and 23 °manifest the C/2m super structure derived from the Li_2MnO_3 component for both the materials. Additionally, the intensity ratio of I(003)/I(104) reflections is clearly higher than 1.2 (1.32 for LRNM-S and 1.82 for LRNM-A). Also, the clear peak separation of the (108)/(110) reflections at around $2\theta = 65°$ confirms the targeted layered structure without spinel impurities. These evidences indicate well crystallized materials, which detailed structural and crystallographic information, obtained from Rietveld refinement, is summarized in Table 2 (detailed structural parameters given in Tables S1 and S2 in Supporting Information).

The ratio of the crystallographic lattice parameters *a* and *c* (Table 2) in terms of *c/3a* results in a value of 1.66 for both samples indicating complete formation of the layered structure [32,33]. Importantly, the lattice parameters of LRNM-S and LRNM-A are practically identical indicating that the choice of reactants for the co-precipitation does not significantly affect the crystal structure of the presented final material, $Li_{1.2}Ni_{0.2}Mn_{0.6}O_2$. The degree of cation mixing, i.e. Ni^{2+} ions in Li^+ sites of the interlayer, is also fairly similar, being 6 % for LRNM-S and 5 % for LRNM-A. However, the crystallite size is distinctively different with 130 nm for LRNM-S and 224 nm for LRNM-A, supporting the SEM observations indicating much larger primary particles for the latter material. Overall, the structural and morphological analysis confirm that both materials share the layered structure with almost identical lattice parameters and cation mixing levels regardless of the transition metal species used for precursor synthesis, but distinctively different primary particle and crystallite sizes.

The differences in chemical composition (Li:TM ratio) and primary particle/crystallite size are directly reflected in the potential profiles of the two LRNM materials showing different redox contributions during the first dis-/charge cycle. The dashed line in Fig. 2(a) indicates the threshold (identified as the minimum from the differential capacity plot of Fig. 2(b)) between the sloping region associated to the 'classical' Ni-redox activity and the extended high-voltage plateau ascribed to the activation of the Li_2MnO_3 component, which involves partially

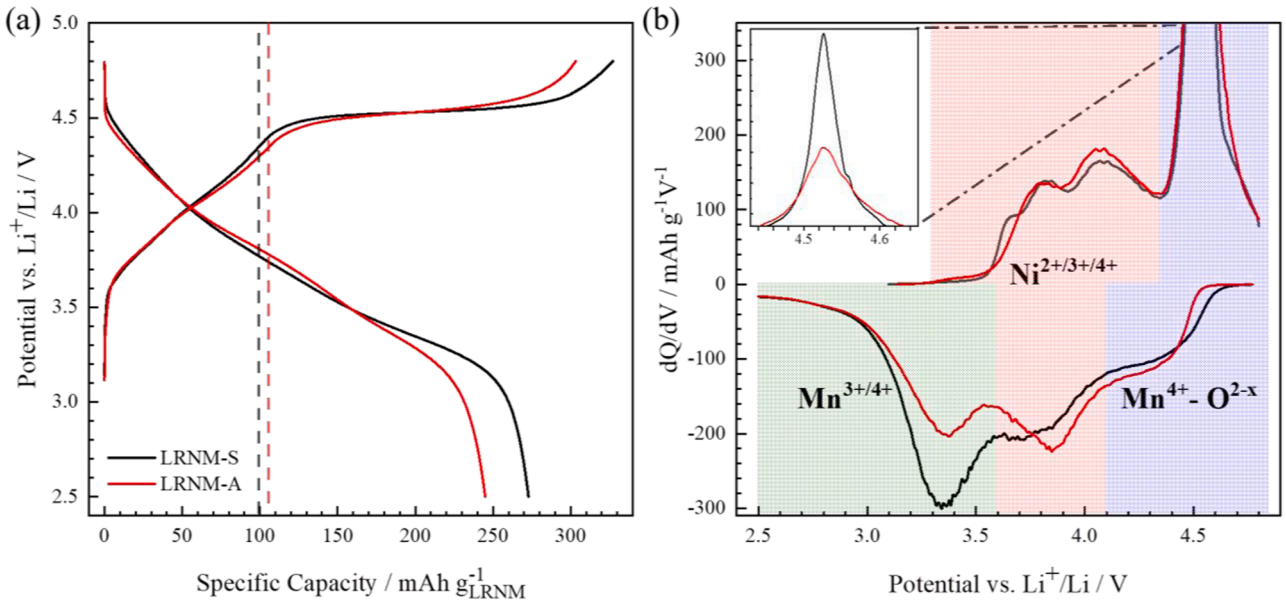

Fig. 2. (a) Potential profiles and (b) the differential capacity plots for the first cycle at C/20 of LRNM-S and LRNM-A.

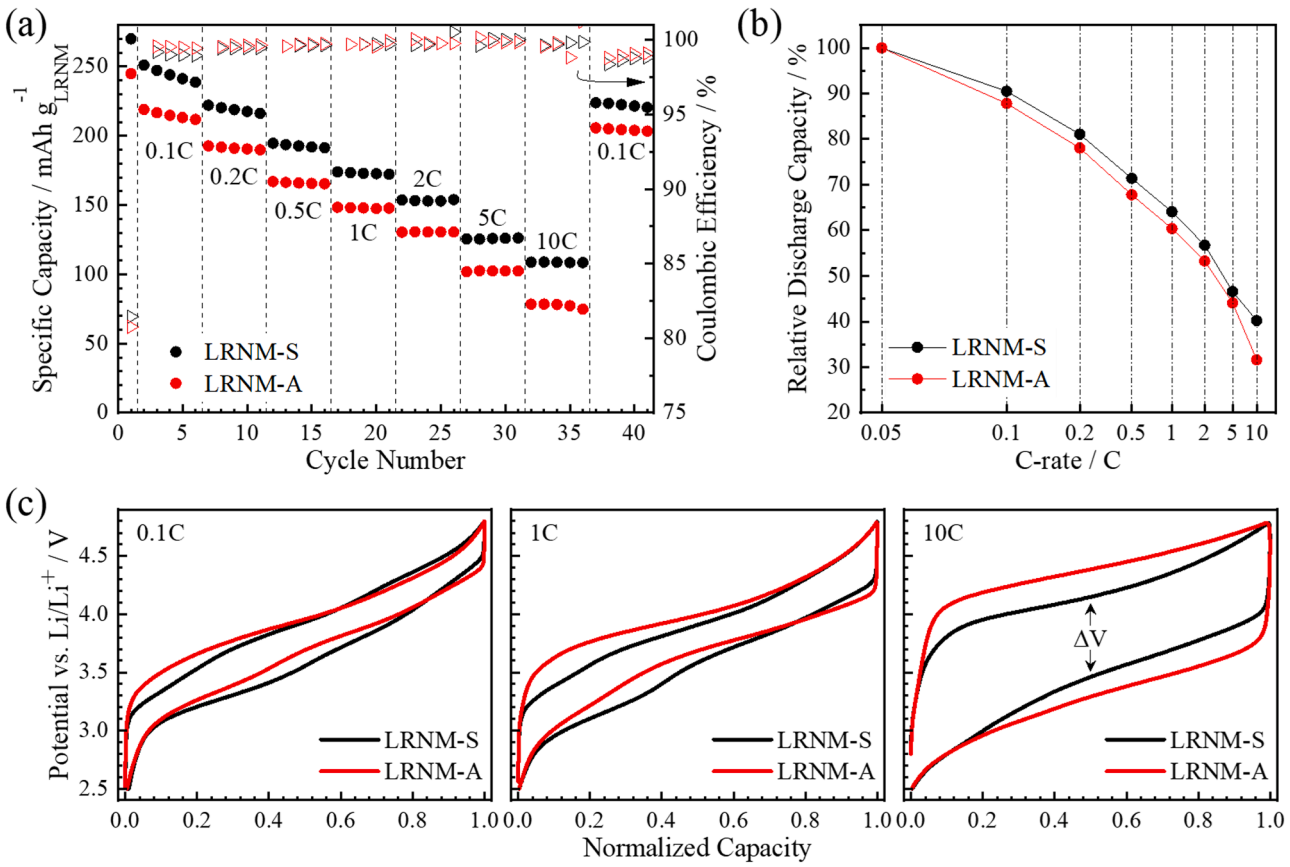

Fig. 3. (a) Rate capability test of LRNM-S and LRNM-A, (b) Relative discharge specific capacity at different C-rate to the specific capacity at 0.05C, (c) Normalized potential profiles of LRNM-S and LRNM-A at dis-/charge rates of 0.1C, 1C and 10C.

irreversible anion redox [34]. As expected from the slightly higher stoichiometry of TMs (Table 1), LRNM-A displays a slightly higher capacity in the sloping region compared to LRNM-S (106 mAh g^{-1} vs. 100 mAh g^{-1}), but a lower capacity along the high-voltage plateau (197 mAh g^{-1} vs. 227 mAh g^{-1}). The higher nickel content in LRNM-A (Table 1) is also reflected in the discharge potential curve and the corresponding feature for $Ni^{4+/3+/2+}$ reduction at around ~3.8 V, which appears more pronounced also in the dQ/dV plot of Fig. 2(b). Nevertheless, most of the difference in charge capacity between the two LRNMs originates from the high-voltage plateau (~35 mAh g^{-1}). At the same time, LRNM-S shows higher reversibility than LRNM-A with an initial Coulombic efficiency of ~81.4 % compared to 80.6 %. Interestingly, the dQ/dV features upon discharge of LRNM-S and LRNM-A are very similar to those reported for $xLi_2MnO_3•(1-x)LiMn_{0.5}Ni_{0.5}O_2$) LRLOs with higher (x = 0.5) and lower (x = 0.3) Li_2MnO_3 contents [35], or when LRLOs are activated at lower or higher specific currents [34], respectively. In fact, both (larger proportion of Li_2MnO_3 and/or activation at lower currents) would lead to a much stronger Mn-related feature at around 3.3–3.4 V in the dQ/dV curve during discharge. Since the stoichiometry of LRNM-S and LRNM-A are rather similar and the cycling test conditions are the same, the strongest peaks in the dQ/dV plot of Fig. 2(b), (i.e., above 4.5 V during oxidation and below 3.5 V during reduction) point towards a more complete utilization of the Li_2MnO_3 component, i.e., a more reversible oxygen redox in LRNM-S. The reason for this behavior resides in the morphology of the positive electrode materials. LRNM-S is composed of smaller primary particles (and crystallites), hence, larger specific surface area which enables a larger fraction of active material to participate in the electrochemical reaction. In this regard, it is well-known that nano-sized primary particles enhance the performance of different LIB electrode materials such as $LiFePO_4$ [36,37] and $Li_4Ti_5O_{12}$ [38,39] through very short Li^+ diffusion pathways. Since LRLOs have indeed low electronic conductivity as compared to other positive electrode materials, i.e., Co-containing layered oxides, the different size of primary particles may have a significant impact on the performance.

To examine the effect of particle size on the electrochemical properties in more detail, we first investigated the rate capability and voltage hysteresis for the two LRNM materials at different dis/-charge rates (Fig. 3). The above-mentioned difference in specific discharge capacity of LRNM-S and LRNM-A is maintained across all rates as it can be seen from the plot in Fig. 3(a). Interestingly, the difference between the two samples increases with the rate. At 10C, LRNM-S delivers 109 mAh g^{-1} compared to 77 mAh g^{-1} for LRNM-A (averaged over 5 cycles, individual potential profiles shown in Figure S1 of the Supporting Information). The smaller LRNM-S primary particles enable higher capacities at every current density as it is clear in the plot of normalized capacity (vs. the first cycle at C/20) at different rates (Fig. 3(b)).

Besides the specific capacity at different rates, the voltage hysteresis (ΔV) between charge and discharge, is another key factor influencing the energy storage performance of the system, directly translating into heat loss/evolution especially at high dis-/charge currents. Fig. 3(c) compares the normalized charge and discharge potential profiles of LRNM-S and LRNM-A at very low (0.1C), medium (1C) and very high (10C) rates. At lower dis-/charge rates of 0.1C and 1C similar voltage hysteresis are observed for both LRNM-S and LRNM-A, being obviously higher at 1C. However, at 10C rate a significant voltage hysteresis, higher than 1.1 V is observed for LRNM-A, while LRNM-S shows less than 0.8V difference. This once more highlights the benefit of the LRNM-S smaller particles to enable high energy efficiency in addition to high capacity at high dis-/charge rates.

Despite the improved electrochemical properties of LRNM-S described so far, the smaller primary particles seemingly have a

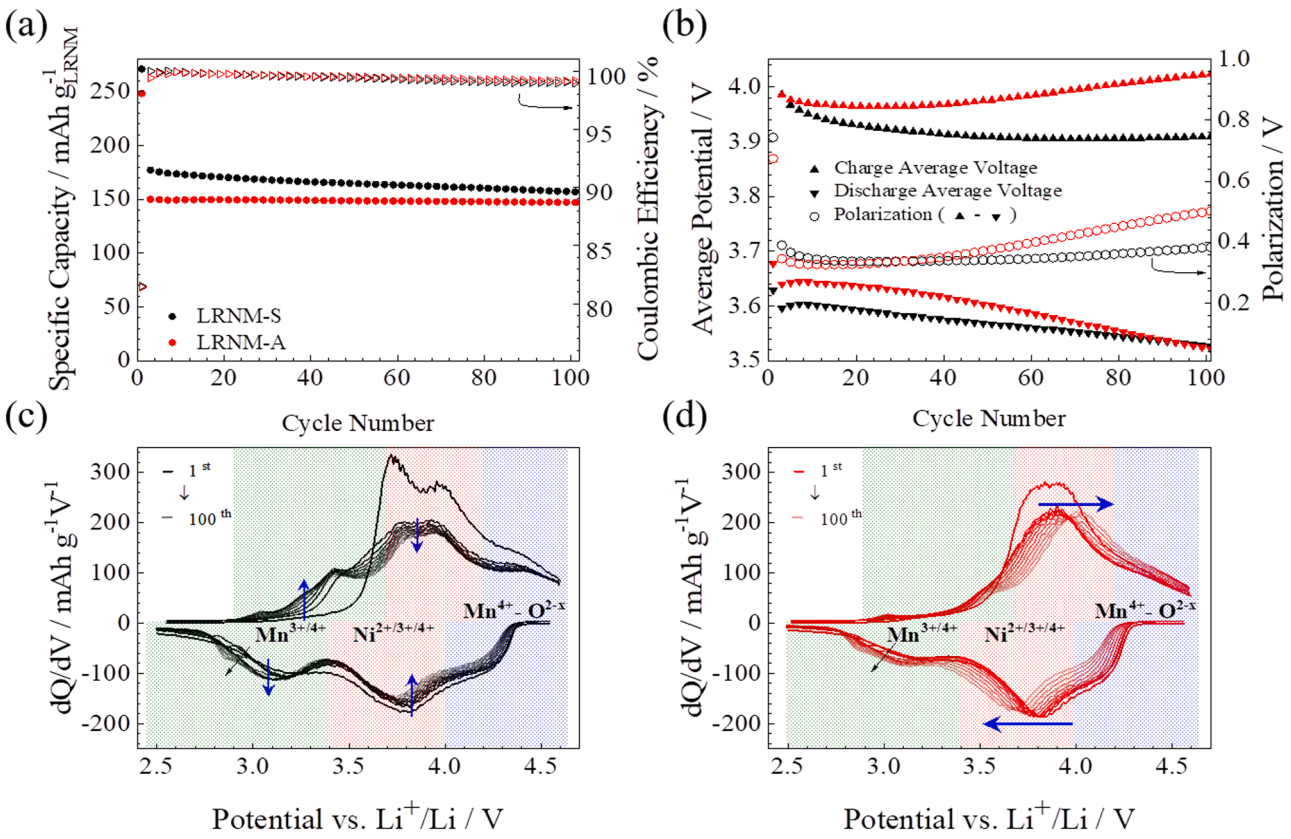

Fig. 4. Galvanostatic cycling stability tests of LRNM-S and LRNM-A (at 1C) following the activation cycle at C/20. Evolution of (a) specific discharge capacity and (b) average discharge voltage. Selected (every tenth cycle) differential specific capacity plots of (c) LRNM-S and (d) LRNM-A.

detrimental impact on cycling stability as indicated by the stronger capacity fading during the long-term cycle test at 0.1C in Fig. 3(a). This becomes even more clear comparing the galvanostatic cycling data presented in Fig. 4. During the initial cycle at 1C, LRNM-S offers a much higher discharge capacity (179 mAh g^{-1}) than LRNM-A (151 mAh g^{-1}). Over 100 cycles, however, LRNM-S shows a relatively poor capacity retention (88%) dropping to 157 mAh g^{-1} while LRNM-A maintains nearly 97 % of its initial capacity delivering 147 mAh g^{-1}. Interestingly, the evolution of average (dis)charge potentials and polarization or voltage hysteresis (ΔV) for the two materials show a very different behavior. Initially, LRNM-A has a higher average working potential (~3.64 V) than LRNM-S (3.60 V), however, after 100 cycles they approach a similar value at around 3.53 V as shown in Fig. 4(b). This translates into a retention of the average discharge potential over 100 cycles of 98 % and 97 % for LRNM-S and LRNM-A, respectively. At the same time the respective average charge potentials show a very different behavior: For LRNM-A it increases at a similar rate as discharge voltage decreases, leading to a rather rapid increase of the voltage hysteresis between charge and discharge rising from ~0.3V initially, to 0.5V after 100 cycles at 1C. In contrast, the average charge potential of LRNM-S also decreases upon cycling resulting in a rather stable voltage hysteresis (0.35–0.40 V) throughout 100 cycles. This points towards two fundamentally different ageing mechanisms dominating the two materials, which differ only in particle and crystallite size. To investigate the working potential fading, the differential capacity plots of every 10th cycle at 1C of LRNM-S and LRNM-A are compared in Fig. 4(c) and (d), respectively (the normalized potential profiles are shown in Fig. S2 of the Supporting Information). A clear difference is observed in the differential capacity plots of the two materials nicely revealing the different ageing mechanisms between the 1st and 100th cycle. The smaller particles and crystallites of LRNM-S display the typical shift of redox activity from the mid-to-higher-voltage region (3.7–4.2V) to the lower-voltage region (2.5–3.7V), known as 'voltage fading' from the early studies of Thackeray and co-workers [35,40]. Despite the remaining ambiguity [35,41–43], there is consensus among the scientific literature that the voltage fading is the consequence of the irreversible TM migration in the LRLOs, which is closely coupled to oxygen redox activity, causing structural transformation or degradation [44]. On the other hand, there is also a reversible portion of TM migration, as well proposed by Thackeray et al. [40], which is responsible for the voltage hysteresis between charge and discharge and when finely tuned even beneficial to maintain a stable oxygen redox contribution [43,45], i.e., stable high capacity. This is what is found from the differential capacity plots of LRNM-A, where the shift of capacities is not observed, but rather a shift of the persistent peaks to higher and lower potentials during charge and discharge respectively, resulting in the increased polarization or voltage hysteresis. The continuous increase in polarization for LRNM-A might therefore be the combination of several phenomena such as the partially irreversible TM migration into the Li layer, i.e., the cation mixing, electrolyte side reactions, and surface film formation on the aged active material particles.

To further investigate and confirm the different ageing mechanisms an *ex-situ* XRD and XPS analysis on cycled electrodes was performed. The diffraction patterns of cycled electrodes are compared to the pristine electrode at selected 2θ ranges (Fig. 5). Within each range, the intensities were rescaled to facilitate the comparison of the structural changes. After cycling, a shift of the strongest (003) reflection to lower 2θ angles can be observed for both materials. Other reflections show a similar trend indicating the lattice expansion in *c*-direction, which is the result of the increased repulsion of the TM slabs due to the irreversible loss of lithium after activation. As expected, the super structure peaks of the Li_2MnO_3 phase of C2/m structure, i.e., (110) and (020) reflections, have disappeared in both samples. Overall, the peak shift after 100 cycles is much stronger for LRNM-S, e.g., see the (101) and (104)

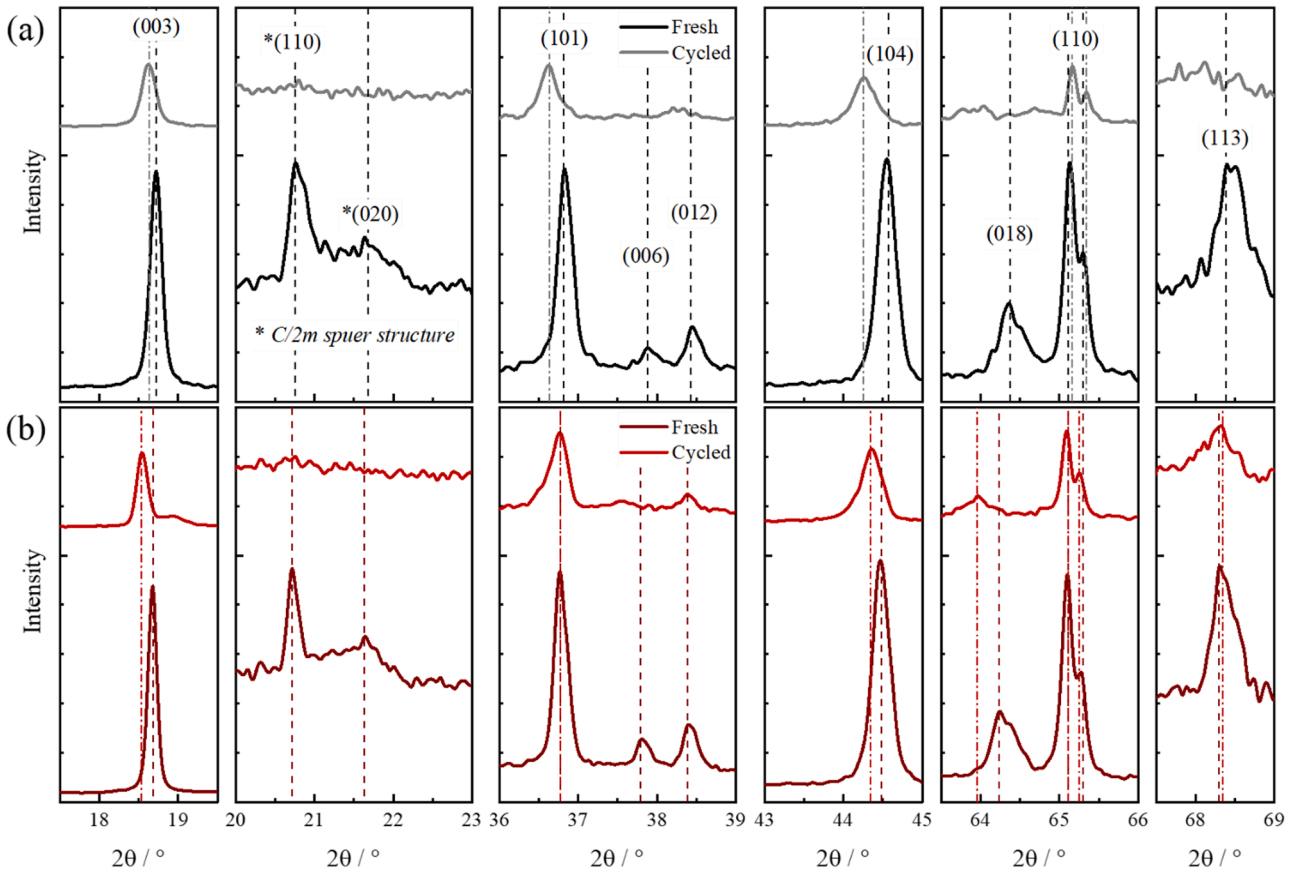

Fig. 5. *Ex-situ* XRD patterns of (a) LRNM-S and (b) LRNM-A recorded for pristine (fresh) and cycled (100 cycles) electrodes.

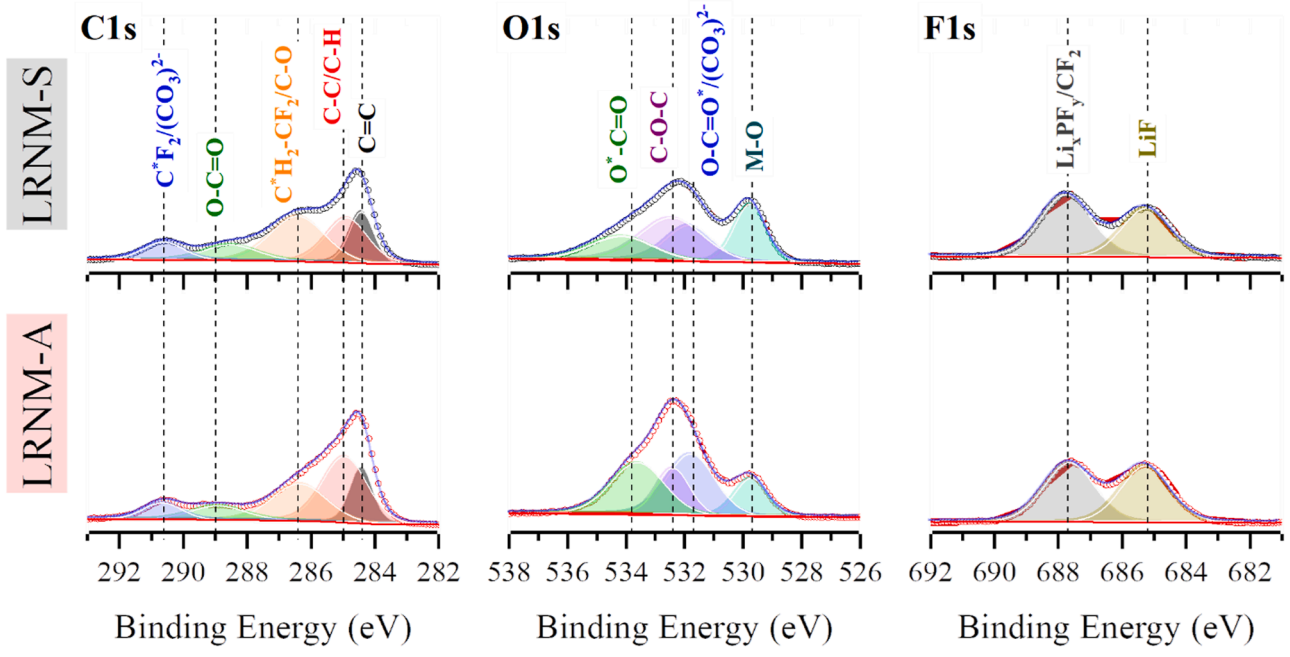

Fig. 6. *Ex-situ* XPS spectra of LRNM-S and LRNM-A electrodes after 100 cycles at 1C rate.

reflections, while those shifts are almost negligible for LRNM-A. In addition, the intensities of LRNM-S have decreased much stronger than those of LRNM-A. Certain reflections, e.g., (006), (018) and (113), even vanished, in line with the more rapid structural degradation of LRNM-S.

On the other hand, the XPS spectra (Fig. 6) show no significant differences in surface composition among the two samples with very similar features in the C1s, O1s and F1s region. For both materials, the C1s region shows the C═C (284.4 eV) and C—C/C—H (285.0 eV) peaks corresponding to conductive carbon (Super C65), a peak around 286.4 eV mainly due to C—O moieties and a contribution from the CH_2—CF_2

groups of the PVdF binder. The peak at 289.0 eV is attributed to alkyl-carbonate groups (O—C═O), e.g., from the carbonate-based solvents. Finally, the CF_2 peak at 290.6 eV is another signal of PVdF binder as well as overlapped carbonate species ($(CO_3)_2^-$). The O—C═O peaks, as well as the C—O—C peak are also present in the O1s spectra, and, very similarly for both materials, centered around 531.7 eV and 533.8 eV as well as at 532.4 eV, respectively. On the contrary, the intensity ratio between the metal oxide (M—O) peak (529.7 eV) coming from the active material to those organic (and carbonate) species peaks is significantly decreased in LRNM-A compared to LRNM-S. This larger deviation for LRNM-A is a good indicator of a thicker cathode electrolyte interphase (CEI) layer on the LRNM-A electrode. In fact, the same trend is observed in the F1s spectrum of LRNM-A, presenting a relatively higher intensity of the LiF peak at ~685.5 eV resulting from the decomposition of $LiPF_6$. Considering the M-O peak reduction (O1s region) and the higher LiF intensity (F1s region), a thicker CEI layer might be the reason for the continuous increase in electrode polarization and voltage hysteresis of the LRNM-A electrodes upon cycling.

All in all, the *ex-situ* measurements clearly confirm that LRNM-A is structurally more stable upon long-term cycling, in good agreement with its high capacity retention and low voltage fading. The co-precipitation via TM acetates leads to large primary crystallites for LRNM-A, in which the Li_2MnO_3 is activated to a low extent. Therefore, the material only shows ageing in terms of increasing voltage hysteresis due to increased cation mixing, i.e., Ni^{2+} ion trapping in Li sites, which slowly increases with cycling. On the other hand, the severe discharge capacity degradation of LRNM-S results from the strong degradation of the crystalline structure, confirmed by *ex-situ* XRD measurements, due to the extensive activation of Li_2MnO_3. In this material, the dominating degradation mechanism is the 'structural voltage fading' proposed by Thackeray and co-workers [35], which becomes more pronounced with the increasing (active) fraction of the Li_2MnO_3 component [35,40]. Thus, the different particle and crystallite size of the two materials determines the long-term material performance.

4. Conclusions

LRNM active materials have been synthesized from transition metal precursors with different anions, i.e. $(TM(II)SO_4 \bullet nH_2O$ and $TM(II)(CH_3COO)_2 \bullet nH_2O)$, via otherwise identical co-precipitation and solid-state reaction. The choice of the anion strongly affects the morphological features of the resulting LRNMs, leading to different primary particles size. This difference results in rather different electrochemical performance. The smaller crystallite size of LRNM-S results in much higher specific capacity upon the initial activation and superior rate capability, i.e., more than 100 mAh g^{-1} at 10C. However, upon long-term cycling, LRNM-A offers better stability in terms of voltage profile and, especially, capacity retention (97% vs 88%), than LRNM-S. The first cycle differential capacity profiles reveal that the reason for the increased capacity of LRNM-S is a stronger contribution of the Li_2MnO_3 component [35,40], i.e., an increased proportion of oxygen redox. However, this is directly coupled to increased irreversible TM migration leading to the material's structural degradation and the typical 'voltage fading' as evidenced by *ex-situ* XRD and electrochemical results. On the other hand, the nearly twice as large primary crystallites of LRNM-A follow a different, less severe degradation mechanism dominated by only an increasing of voltage hysteresis and polarization as evidenced by the very different evolution of differential capacity profiles compared to LRNM-S. Overall, the results suggest that the fine tuning between reversible TM migration (voltage hysteresis) and full utilization of oxygen redox (coupled to irreversible TM migration and voltage fading) needs to be found to achieve optimized LRLO materials. Besides stoichiometry, structure and structural doping – primary particle and crystallite size can play a key role in this.

Authors' contributions

H.C. performed the material synthesis and basic XRD characterization, electrochemical and physicochemical measurements, and drafted the manuscript. A.S. performed the refinement of the XRD measurements. H.M. performed and analyzed the XPS measurements with H.C. M.K. conceptualized the activities, supervised the experimental work and the writing of the manuscript. S.P. conceptualized and coordinated the activities, provided funding for the work, and revised the manuscript.

Declaration of Competing Interest

The authors declare that they have no known competing financial interests or personal relationships that could have appeared to influence the work reported in this paper.

Acknowledgments

The authors would like to acknowledge financial support from the European Union within the Si-DRIVE project. This project has received funding from the European Union's Horizon 2020 research and innovation programme under grant agreement No 814464. The financial support of the Helmholtz Association is also acknowledged.

Supplementary materials

Supplementary material associated with this article can be found, in the online version, at doi:10.1016/j.electacta.2022.141047.

References

[1] M.S. Whittingham, Lithium batteries and cathode materials, Chem. Rev. 104 (10) (2004) 4271–4301, https://doi.org/10.1021/cr020731c.
[2] J.-M. Tarascon, M. Armand, Issues and challenges facing rechargeable lithium batteries, Nature 414 (6861) (2001) 359–367, https://doi.org/10.1038/35104644.
[3] N. Nitta, F. Wu, J.T. Lee, G. Yushin, Li-ion battery materials: present and future, Mater. Today 18 (5) (2015) 252–264, https://doi.org/10.1016/j.mattod.2014.10.040.
[4] C. Daniel, D. Mohanty, J. Li, D.L. Wood, Cathode materials review, AIP Conf. Proc. 1597 (2014) 26–43, https://doi.org/10.1063/1.4878478.
[5] Y. Zhang, Y. Li, X. Xia, X. Wang, C. Gu, J. Tu, High-energy cathode materials for Li-ion batteries: a review of recent developments, Sci. China Technol. Sci. 58 (11) (2015) 1809–1828, https://doi.org/10.1007/s11431-015-5933-x.
[6] M. Li, J. Lu, Cobalt in lithium-ion batteries, Science 367 (6481) (2020) 979–980, https://doi.org/10.1126/science.aba9168.
[7] C.B.L. Nkulu, L. Casas, V. Haufroid, T.D. Putter, N.D. Saenen, T. Kayembe-Kitenge, P.M. Obadia, D.K.W. Mukoma, J-M.L. Ilunga, T.S. Nawrot, O.L. Numbi, E. Smolders, B. Nemery, et al., Sustainability of artisanal mining of cobalt in DR Congo, Nat. Sustain. 1 (9) (2018) 495–504, https://doi.org/10.1038/s41893-018-0139-4.
[8] X. Fu, D.N. Beatty, G.G. Gaustad, G. Ceder, R. Roth, R.E. Kirchain, M. Bustamante, C. Babbitt, E.A. Olivetti, Perspectives on cobalt supply through 2030 in the face of changing demand, Environ. Sci. Technol. 54 (5) (2020) 2985–2993, https://doi.org/10.1021/acs.est.9b04975.
[9] X. Zeng, M. Li, D.A. El-Hady, W. Alshitari, A.S. Al-Bogami, J. Lu, K. Amine, Commercialization of lithium battery technologies for electric vehicles, Adv. Energy Mater. 9 (27) (2019) 1900161, https://doi.org/10.1002/aenm.201900161.
[10] F. Wu, G-T. Kim, T. Diemant, M. Kuenzel, A.R. Schür, X. Gao, B. Qin, D. Alwast, Z. Jusys, R.J. Behm, D. Geiger, U. Kaiser, S. Passerini, Reducing capacity and voltage decay of co-free $Li_{1.2}Ni_{0.2}Mn_{0.6}O_2$ as positive electrode material for lithium batteries employing an ionic liquid-based electrolyte, Adv. Energy Mater. 10 (34) (2020) 2001830, https://doi.org/10.1002/aenm.202001830.
[11] P. Rozier, J.M. Tarascon, Review—Li-rich layered oxide cathodes for next-generation Li-ion batteries: chances and challenges, J. Electrochem. Soc. 162 (14) (2015) A2490–A2499, https://doi.org/10.1149/2.0111514jes.
[12] J. Yan, X. Liu, B. Li, Recent progress in Li-rich layered oxides as cathode materials for Li-ion batteries, RSC Adv. 4 (108) (2014) 63268–63284, https://doi.org/10.1039/c4ra12454e.
[13] H. Pan, S. Zhang, J. Chen, M. Gao, Y. Liu, T. Zhu, Y. Jiang, Li- and Mn-rich layered oxide cathode materials for lithium-ion batteries: a review from fundamentals to research progress and applications, Mol. Syst. Des. Eng. 3 (5) (2018) 748–803, https://doi.org/10.1039/C8ME00025E.
[14] J. Zheng, S. Myeong, W. Cho, P. Yan, J. Xiao, C. Wang, J. Cho, J-G. Zhang, Li- and Mn-Rich cathode materials: challenges to commercialization, Adv. Energy Mater. 7 (6) (2017) 1601284, https://doi.org/10.1002/aenm.201601284.

[15] A.R. Armstrong, M. Holzapfel, P. Novák, C.S. Johnson, S-H. Kang, M.M. Thackeray, P.G. Bruce, Demonstrating oxygen loss and associated structural reorganization in the lithium battery cathode Li[$Ni_{0.2}$ $Li_{0.2}$ $Mn_{0.6}$]O_2, J. Am. Chem. Soc. 128 (26) (2006) 8694–8698, https://doi.org/10.1021/ja062027+.

[16] C.S. Johnson, J-S. Kim, C. Lefief, N. Li, J.T. Vaughey, M.M. Thackeray, The significance of the Li_2MnO_3 component in 'composite' xLi_2MnO_3•(1-x) $LiMn_{0.5}Ni_{0.5}O_2$ electrodes, Electrochem. Commun. 6 (10) (2004) 1085–1091, https://doi.org/10.1016/j.elecom.2004.08.002.

[17] M.M. Thackeray, S-H. Kang, C.S. Johnson, J.T. Vaughey, R. Benedek, S.A. Hackney, Li_2MnO_3-stabilized $LiMO_2$ (M = Mn, Ni, Co) electrodes for lithium-ion batteries, J. Mater. Chem. 17 (30) (2007) 3112–3125, https://doi.org/10.1039/b702425h.

[18] F. Amalraj, D. Kovacheva, M. Talianker, L. Zeiri, J. Grinblat, N. Leifer, G. Goobes, B. Markovsky, D. Aurbach, Synthesis of integrated cathode materials xLi_2MnO_3·(1 − x)$LiMn_{1/3}Ni_{1/3}Co_{1/3}O_2$ (x = 0.3 , 0.5 , 0.7) and studies of their electrochemical behavior, J. Electrochem. Soc. 157 (10) (2010) A1121–A1130, https://doi.org/10.1149/1.3463782.

[19] H. Yu, H. Kim, Y. Wang, P. He, D. Asakura, Y. Nakamura, H. Zhou, High-energy 'composite' layered manganese-rich cathode materials via controlling Li_2MnO_3 phase activation for lithium-ion batteries, Phys. Chem. Chem. Phys. 14 (18) (2012) 6584–6595, https://doi.org/10.1039/c2cp40745k.

[20] Z. Lu, J.R. Dahn, Understanding the anomalous capacity of Li/Li [$Ni_xLi_{(1/3-2x/3)}$ $Mn_{(2/3-x/3)}$]O_2 cells using *in situ* x-ray diffraction and electrochemical studies, J. Electrochem. Soc. 149 (7) (2002) A815–A822, https://doi.org/10.1149/1.1480014.

[21] A. Boulineau, L. Simonin, J-F. Colin, E. Canévet, L. Daniel, S. Patoux, Evolutions of $Li_{1.2}Mn_{0.61}Ni_{0.18}Mg_{0.01}O_2$ during the initial charge/discharge cycle studied by advanced electron microscopy, Chem. Mater. 24 (18) (2012) 3558–3566, https://doi.org/10.1021/cm301140g.

[22] D. Mohanty, S. Kalnaus, R.A. Meisner, K.J. Rhodes, J. Li, E.A. Payzant, D.L.W. Ill, C. Daniel, Structural transformation of a lithium-rich $Li_{1.2}Co_{0.1}Mn_{0.55}Ni_{0.15}O_2$ cathode during high voltage cycling resolved by *in situ* X-ray diffraction, J. Power Sources 229 (2013) 239–248, https://doi.org/10.1016/j.jpowsour.2012.11.144.

[23] P.K. Nayak, J. Grinblat, M. Levi, B. Markovsky, D. Aurbach, Structural and electrochemical evidence of layered to spinel phase transformation of Li and Mn rich layered cathode materials of the formulae xLi[$Li_{1/3}$ $Mn_{2/3}$]O_2·(1-x)$LiMn_{1/3}Ni_{1/3}Co_{1/3}O_2$ (x = 0.2, 0.4, 0.6) upon cycling, J. Electrochem. Soc. 161 (10) (2014) A1534–A1547, https://doi.org/10.1149/2.0101410jes.

[24] S. Jouanneau, K.W. Eberman, L.J. Krause, J.R. Dahn, Synthesis, characterization, and electrochemical behavior of improved Li[$Ni_xCo_{1-2x}Mn_x$]O_2 ($0.1 \leq x \leq 0.5$), J. Electrochem. Soc. 150 (12) (2003) A1637–A1642, https://doi.org/10.1149/1.1622956.

[25] J Li, R. Klöpsch, M.C. Stan, S. Nowak, M. Kunze, M. Winter, S. Passerini, Synthesis and electrochemical performance of the high voltage cathode material Li [$Li_{0.2}Mn_{0.56}Ni_{0.16}Co_{0.08}$]$O_2$ with improved rate capability, J. Power Sources 196 (10) (2011) 4821–4825, https://doi.org/10.1016/j.jpowsour.2011.01.006.

[26] A. Kazzazi, D. Bresser, A. Birrozzi, J.v. Zamory, M. Hekmatfar, S. Passerini, Comparative analysis of aqueous binders for high-energy Li-Rich NMC as a lithium-ion cathode and the impact of adding phosphoric acid, ACS Appl. Mater. Interfaces 10 (20) (2018) 17214–17222, https://doi.org/10.1021/acsami.8b03657.

[27] F. Wu, X. Zhang, T. Zhao, L. Li, M. Xie, R. Chen, Multifunctional $ALPO_4$ coating for improving electrochemical properties of low-cost Li[$Li_{0.2}Fe_{0.1}Ni_{0.15}Mn_{0.55}$]$O_2$ cathode materials for lithium-ion batteries, ACS Appl. Mater. Interfaces 7 (6) (2015) 3773–3781, https://doi.org/10.1021/am508579r.

[28] H. Xu, S. Deng, G. Chen, Improved electrochemical performance of $Li_{1.2}Mn_{0.54}Ni_{0.13}Co_{0.13}O_2$ by Mg doping for lithium ion battery cathode material, J. Mater. Chem. A 2 (36) (2014) 15015–15021, https://doi.org/10.1039/C4TA01790K.

[29] P. Yan, J. Zheng, X. Zhang, R. Xu, K. Amine, J. Xiao, J-G. Zhang, C-M. Wang, Atomic to nanoscale investigation of functionalities of an Al_2O_3 coating layer on a cathode for enhanced battery performance, Chem. Mater. 28 (3) (2016) 857–863, https://doi.org/10.1021/acs.chemmater.5b04301.

[30] B. Xu, C.R. Fell, M. Chi, Y.S. Meng, Identifying surface structural changes in layered Li-excess nickel manganese oxides in high voltage lithium ion batteries: a joint experimental and theoretical study, Energy Environ. Sci. 4 (6) (2011) 2223–2233, https://doi.org/10.1039/c1ee01131f.

[31] J. Bréger, M. Jiang, N. Dupre, Y.S. Meng, Y. Shao-Horn, G. Ceder, C.P. Grey, High-resolution X-ray diffraction, DIFFaX, NMR and first principles study of disorder in the Li_2MnO_3-Li[$Ni_{1/2}Mn_{1/2}$]O_2 solid solution, J. Solid State Chem. 178 (9) (2005) 2575–2585, https://doi.org/10.1016/j.jssc.2005.05.027.

[32] C. Yu, H. Wang, X. Guan, J. Zheng, L. Li, Conductivity and electrochemical performance of cathode xLi_2MnO_3•(1 -X)$LiMn_{1/3}Ni_{1/3}Co_{1/3}O_2$ (x = 0.1, 0.2, 0.3, 0.4) at different temperatures, J. Alloys Compd. 546 (2013) 239–245, https://doi.org/10.1016/j.jallcom.2012.08.026.

[33] Q. Wang, W. He, L. Wang, S. Li, H. Zheng, Q. Liu, Y. Cai, J. Lin, Q. Xie, D-P. Peng, Morphology control and Na^+ doping toward high-performance Li-Rich layered cathode materials for lithium-ion batteries, ACS Sustain. Chem. Eng. 9 (1) (2021) 197–206, https://doi.org/10.1021/acssuschemeng.0c06595.

[34] J. Wang, X. He, E. Paillard, N. Laszczynski, J. Li, S. Passerini, Lithium- and manganese-rich oxide cathode materials for high-energy lithium ion batteries, Adv. Energy Mater. 6 (21) (2016) 1600906, https://doi.org/10.1002/aenm.201600906.

[35] J.R. Croy, K.G. Gallagher, M. Balasubramanian, B.R. Long, M.M. Thackeraya, Quantifying hysteresis and voltage fade in xLi_2MnO_3·(1-x)$LiMn_{0.5}Ni_{0.5}O_2$ electrodes as a function of Li_2MnO_3 content, J. Electrochem. Soc. 161 (3) (2014) 318–325, https://doi.org/10.1149/2.049403jes.

[36] X. Guo, B. Song, G. Yu, X. Wu, X. Feng, D. Li, Y. Chen, Size-dependent memory effect of the $LiFePO_4$ electrode in Li-ion batteries, ACS Appl. Mater. Interfaces 10 (48) (2018) 41407–41414, https://doi.org/10.1021/acsami.8b15933.

[37] N. Zhao, Y. Li, X. Zhao, X. Zhi, G. Liang, Effect of particle size and purity on the low temperature electrochemical performance of $LiFePO_4$/C cathode material, J. Alloys Compd. 683 (2016) 123–132, https://doi.org/10.1016/j.jallcom.2016.04.070.

[38] Y. Shen, J.R. Eltzholtz, B.B. Iversen, Controlling size, crystallinity, and electrochemical performance of Li $_4Ti_5O_{12}$ nanocrystals, Chem. Mater. 25 (24) (2013) 5023–5030, https://doi.org/10.1021/cm402366y.

[39] E. Pohjalainen, T. Rauhala, M. Valkeapää, J. Kallioinen, T. Kallio, Effect of $Li_4Ti_5O_{12}$ particle size on the performance of lithium ion battery electrodes at high C-rates and low temperatures, J. Phys. Chem. C 119 (5) (2015) 2277–2283, https://doi.org/10.1021/jp509428c.

[40] K.G. Gallagher, J.R. Croy, M. Balasubramanian, M. Bettge, D.P. Abraham, A. K. Burrell, M.M. Thackeray, Correlating hysteresis and voltage fade in lithium- and manganese-rich layered transition-metal oxide electrodes, Electrochem. Commun. 33 (2013) 96–98, https://doi.org/10.1016/j.elecom.2013.04.022.

[41] X. Yu, Y. Lyu, L. Gu, H. Wu, S-M. Bak, Y. Zhou, K. Amine, S.N. Ehrlich, H. Li, K-W. Nam, X-Q. Yang, Understanding the rate capability of high-energy-density Li-rich layered $Li_{1.2}Ni_{0.15}Co_{0.1}Mn_{0.55}O_2$ cathode materials, Adv. Energy Mater. 4 (5) (2014) 1300950, https://doi.org/10.1002/aenm.201300950.

[42] A.K. Shukla, Q.M. Ramasse, C. Ophus, H. Duncan, F. Hage, G. Chen, Unravelling structural ambiguities in lithium- and manganese-rich transition metal oxides, Nat. Commun. 6 (1) (2015) 8711, https://doi.org/10.1038/ncomms9711.

[43] W.E. Gent, K. Lim, Y. Liang, Q. Li, T. Barnes, S-J. Ahn, K.H. Stone, M. McIntire, J. Hong, J.H. Song, Y. Li, A. Mehta, S. Ermon, T. Tyliszczak, D. Kilcoyne, D. Vine, J-H. Park, S-K. Doo, M.F. Toney, W. Yang, D. Prendergast, W.C. Chueh, Coupling between oxygen redox and cation migration explains unusual electrochemistry in lithium-rich layered oxides, Nat. Commun. 8 (1) (2017) 2091, https://doi.org/10.1038/s41467-017-02041-x.

[44] M. Sathiya, A.M. Abakumov, D. Foix, G. Rousse, K. Ramesha, M. Saubanère, M. L. Doublet, H. Vezin, C.P. Laisa, A.S. Prakash, D. Gonbeau, G. VanTendeloo, J-M. Tarascon, Origin of voltage decay in high-capacity layered oxide electrodes, Nat. Mater. 14 (2) (2015) 230–238, https://doi.org/10.1038/nmat4137.

[45] D. Eum, B. Kim, S.J. Kim, H. Park, J. Wu, S-P. Cho, G. Yoon, M.H. Lee, S-K. Jung, W. Yang, W.M. Seong, K. Ku, O. Tamwattana, S.K. Park, I. Hwang, K. Kang, Voltage decay and redox asymmetry mitigation by reversible cation migration in lithium-rich layered oxide electrodes, Nat. Mater. 19 (4) (2020) 419–427, https://doi.org/10.1038/s41563-019-0572-4.